Structures 11 (2017) 146–154

Contents lists available at ScienceDirect

Structures

journal homepage: www.elsevier.com/locate/structures

Moment-Curvature-Thrust Relationships for Beam-Columns

Andrew Liew[a,*], Leroy Gardner[b], Philippe Block[a]

[a] Institute of Technology in Architecture, ETH Zurich, Switzerland
[b] Department of Civil and Environmental Engineering, Imperial College London, United Kingdom

ARTICLE INFO

Keywords:
Moment curvature thrust
Curves
Cross-section
Metal
Beam
Column
Plated
Hollow sections

ABSTRACT

Moment–curvature–thrust relationships (M–κ–N) are a useful resource for the solution of a variety of inelastic and geometrically non-linear structural problems involving elements under combined axial load and bending. A numerical discretised cross-section method is used in this research to generate such relationships for I-sections, rectangular box-sections and circular or elliptical hollow sections. The method is strain driven, with the maximum strain limited by an a priori defined local buckling strain, which can occur above or below the yield strain depending on the local slenderness of the cross-section. The relationship between the limiting strain and the local slenderness has been given for aluminium, mild steel and stainless steel cross-sections through the base curve of the Continuous Strength Method. Moment-curvature-thrust curves are derived from axial force and bending moment interaction curves by pairing the curvatures and moments for a given axial load level. These moment–curvature–thrust curves can be transformed into various formats to solve a variety of structural problems. The gradient of the curves is used to find the materially and geometrically non-linear solution of an example beam-column, by solving numerically the moment–curvature ordinary differential equations. The results capture the importance of the second order effects, particularly with regard to the plastic hinge formation at mid-height and the post-peak unloading response.

1. Introduction

For a given cross-section, such as an open or closed metal I-section or tubular section, moment–curvature (M–κ) curves can be created. Such curves can be used to describe the behaviour of each cross-section and subsequently the entire length of a structural member, subjected to a given applied load. Generating the M–κ curve is straightforward when there is no applied axial load, since the strains throughout the cross-section are exclusive to flexure, which can be described as linearly varying with depth, with the highest strains at the outer fibres. This is based on the assumption that plane sections remain plane during bending, which has been shown to be valid for practical structural steel cross-sections in bending, as determined from strain gauge readings on I-sections up to and beyond the plastic moment [1]. This also stems from the fact that cross-section dimensions are generally considerably smaller than beam lengths, permitting the neglect of shear deformations [2]. Combining this assumed strain profile with a particular material model, M–κ curves can be generated analytically.

The determination of M–κ curves in the presence of a given axial load is more challenging, due to the interaction between the axial and bending strains and material non-linearity. Expressions for solid rectangular sections with an elastic-perfectly plastic material model can be found in [2], which also describes other approximations for different cross-section shapes. Finding accurate analytical curves for cross-section shapes typically used in structural applications and with more realistic material stress–strain curves is significantly more challenging as a continuous function is needed in the entire M–κ–N domain, that is initially straight in the elastic region and then transitions through to a curved shape in the inelastic regime. The calculation and application of moment–curvature–thrust relationships in the literature include: steel reinforced rectangular masonry sections using non-linear constitutive models [3]; moment–curvature relationships for various tubular cross-sections with residual stresses, geometric imperfections and hydrostatic pressures via the tangent stiffness Newmark method in [4]; using M–κ–N curves to analyse the ultimate strength of dented tubular members by [5]; creating curves by results from finite element analyses as in [6]; non-linear analyses of reinforced concrete beams considering tension softening and bond slip using moment–curvature curves from a section analysis in [7]; moment–curvature curves and comparisons with experimental results of CFRP-strengthened steel circular hollow section beams by [8] and with concrete-filled hollow section tubes [9]. Fibre based models, where the cross-section is discretised into a finite number of thin strips, have been used to model concrete-filled steel tubes [10], as well as the static and dynamic

* Corresponding author at: Institute of Technology in Architecture, Zurich 8093, Switzerland.
E-mail address: liew@arch.ethz.ch (A. Liew).

http://dx.doi.org/10.1016/j.istruc.2017.05.005
Received 21 February 2017; Received in revised form 22 May 2017; Accepted 23 May 2017
Available online 24 May 2017

response of reinforced concrete columns and beam-columns in frames [11,12].

In the present study, a numerical procedure is employed in which cross-section interaction curves are first formed and then used to find all possible strain distributions that correspond to the same axial load level, leading to the required *M–κ–N* curves. The approach is demonstrated for cross-sections with at least one line of symmetry, such as I-sections and tubular sections and for a bi-linear material model, but the method can be used for any cross-section geometry. Key features of the method are that: 1) it is not specific to a particular material model, as any stress–strain curve can be used with the strain driven approach, 2) local buckling of thin-walled elements can be explicitly included through a limiting strain ratio due to the integration with the Continuous Strength Method, 3) any cross-section shape that can be discretised into discrete elements may be analysed, and 4) the procedure allows for efficient calculation of the inelastic flexural stiffness and plastic hinge regions of a member, subjected to given axial load levels.

2. Cross-section model

The central aspects of the cross-section model are described in this section. The cross-section strain and stress distributions are presented in Section 2.1 and a limiting strain is set-out in Section 2.2 to define cross-section failure through local buckling.

2.1. Strain and stress distributions

The strain and stress distributions for a cross-section under axial compression, uni-axial bending and combined axial compression and uni-axial bending are shown in Fig. 1 for the case of a material with a rounded stress–strain relationship.

For the pure axial load state (Fig. 1a), the strains are uniform throughout the cross-section at ϵ_A. When the uniform strain is less than the material yield strain, $\epsilon_A < \epsilon_y$, the cross-section stresses are below f_y, and when $\epsilon_A \geq \epsilon_y$ the cross-section is deforming inelastically according to the chosen material stress–strain curve, up to limiting ultimate values for the cross-section of ϵ_u and f_u.

For the case of simple bending (Fig. 1b), there is no uniform strain present, only linearly-varying flexural strains with a maximum value of ϵ_B. The strain and stress profiles are antisymmetric about the zero strain neutral axis (which is located at mid-depth for symmetric sections), and the upper and lower outer-fibres reach $\pm\,\epsilon_u$ and $\pm\,f_u$.

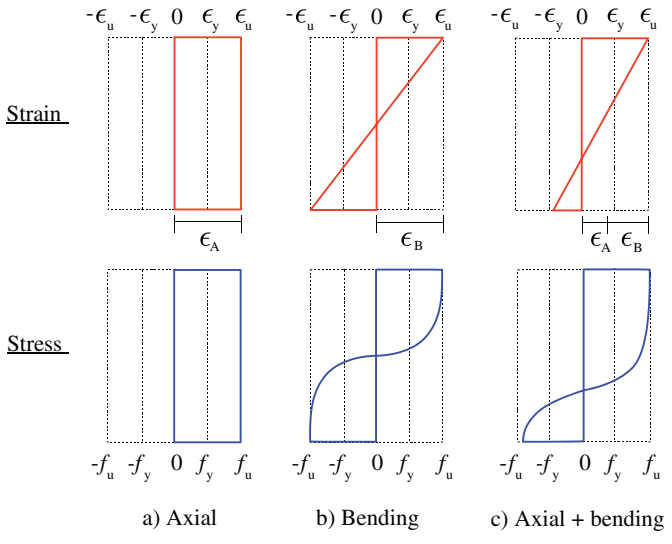

Fig. 1. Cross-section strain and stress distributions under axial compression, uni-axial bending and combined axial compression and uni-axial bending.

The combination of an axial load and bending moment is illustrated in Fig. 1c, where the compressive outer-fibre strain is limited to ϵ_u. The interaction of axial strains and bending strains is taken as the summation of the uniform strains ϵ_A and the linearly varying strains with maximum magnitude ϵ_B. This combination leads to strain and stress profiles between the axial and flexural states. Although strains ϵ_A and ϵ_B are linearly superimposed, the stresses are based on the given material model. Therefore ϵ_A is not solely responsible for defining the axial force and neither is ϵ_B exclusive to bending; it is the combination of ϵ_A and ϵ_B that defines the axial and bending capacity.

The approach adopted herein follows the principles laid-out in research by the first two authors on the deformation-based Continuous Strength Method (CSM) [13,14]. In the CSM, the limiting strain distribution is first established and the stresses and hence capacity follow; this is in contrast to traditional design [15]. The approach described has been used previously to analyse the combined loading (N, M_y, M_z) of cross-sections to produce interaction surfaces and design curves [16].

Since a strain driven approach makes no assumptions on the material model, the same method can be used for a variety of structural materials. This includes metallic construction materials such as structural steel, stainless steel and aluminium, as well as composite construction materials such as reinforced concrete or fibre-reinforced polymers. For cross-sections consisting of two or more materials, the key condition to satisfy for the proposed method, is that there is a compatibility of strains at the interfaces between materials (such as providing full bond to rebar for reinforced concrete cross-sections).

In this research, a simplified bi-linear stress-strain model (Fig. 2) is used based on that recommended for use in numerical models of structural steel elements in [17]. This consists of a linear region with the Young's modulus E up to the yield point f_y, followed by a second linear region with a reduced strain-hardening modulus E_{sh}; the curve is terminated at a specified limiting stress f_u and strain ϵ_u, as described below. Note that $E_{sh} = E/100$ is used throughout this study. This bi-linear material model has been shown to be able to capture the essence of strain hardening in a range of metallic materials, including aluminium and stainless steel, and is used herein for demonstration purposes; this model may however be replaced with a more complex one such as tri-linear, multiple piecewise linear, continuous non-linear or Ramberg-Osgood model, should greater accuracy be sought.

2.2. Strain limits

In strain driven cross-section models, an upper bound must be applied to the strain distribution. This was taken herein as the CSM limiting strain ϵ_{csm} (i.e. $\epsilon_u = \epsilon_{csm}$). The CSM limiting strain ϵ_{csm} is defined as a function of the slenderness of the cross-section $\bar{\lambda}_p$, where

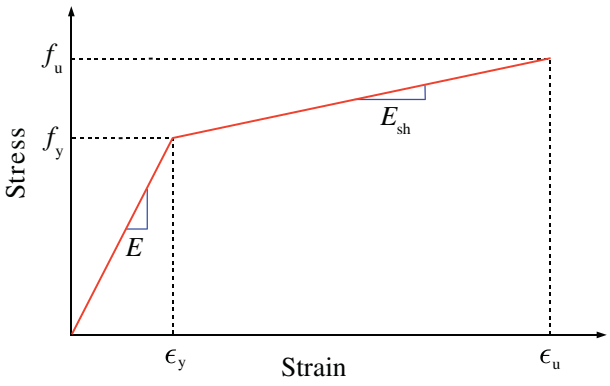

Fig. 2. Bi-linear structural steel material model adopted in this study.

$$\bar{\lambda}_p = \sqrt{\frac{f_y}{\sigma_{cr}}}, \tag{1}$$

with σ_{cr} being the elastic buckling stress of the cross-section. The relationship between $\epsilon_{csm}/\epsilon_y$ and $\bar{\lambda}_p$ is given by a base curve, described by the following equations for plated sections, from which the maximum strain that the cross-section can endure prior to failure by local buckling ϵ_{csm} may be determined.

$$\frac{\epsilon_{csm}}{\epsilon_y} = \frac{0.25}{\bar{\lambda}_p^{3.6}} \le \min\left(15,\ \frac{C_1\epsilon_u}{\epsilon_y}\right) \quad \text{for} \quad \bar{\lambda}_p \le 0.68 \tag{2}$$

$$\frac{\epsilon_{csm}}{\epsilon_y} = \left(1-\frac{0.222}{\bar{\lambda}_p^{1.05}}\right)\frac{1}{\bar{\lambda}_p^{1.05}} \quad \text{for} \quad \bar{\lambda}_p > 0.68 \tag{3}$$

This base curve was derived [13,14,18,19] on the basis of a regression fit to compression and bending test data for a range of metallic materials, including austenitic, duplex and ferritic stainless steels [20], carbon steel [13,18], high strength steel and aluminium [21,22]. An equivalent base curve for circular hollow sections has also been derived [23].

3. Numerical implementation

Although it is possible to derive exact expressions for the combined axial load and uni-axial bending capacity of a cross-section, the results are lengthy for typical cross-sections used in construction and are not generally suitable for practical use. A numerical method is therefore developed to overcome the difficulties in obtaining simple analytical solutions to the interaction of an axial load and bending moment.

The numerical model presented is based on normalising the linearly-varying strain distribution by the limiting cross-section strain ϵ_u. For a given cross-section, all strain interactions are found for which the sum of the uniform strain ϵ_A and the maximum linearly-varying strain ϵ_B equals ϵ_u. To use the same method for axial load and bi-axial bending (N, M_y, M_z), with ϵ_A, ϵ_B and ϵ_C, the reader is directed to [16]. This defines the failure criterion of Eq. (4), which is normalised by the limiting strain as

$$\frac{\epsilon_A}{\epsilon_u} + \frac{\epsilon_B}{\epsilon_u} = 1. \tag{4}$$

The normalised uniform strain ϵ_A/ϵ_u is varied from 0 to 1, indicating pure bending and pure axial loading respectively, and leaving $\epsilon_B/\epsilon_u = 1 - \epsilon_A/\epsilon_u$. This is given by Eq. (5) for major axis bending, where h is the overall cross-section depth and Eq. (6) for minor axis bending where b is the overall cross-section width.

$$\frac{\epsilon_i}{\epsilon_u} = \frac{\epsilon_A}{\epsilon_u} + \left(1-\frac{\epsilon_A}{\epsilon_u}\right)\frac{2y_i}{h}. \tag{5}$$

$$\frac{\epsilon_i}{\epsilon_u} = \frac{\epsilon_A}{\epsilon_u} + \left(1-\frac{\epsilon_A}{\epsilon_u}\right)\frac{2z_i}{b}. \tag{6}$$

With the elemental strains defined, the element stresses are determined from the material model, and hence the cross-section resistances are calculated, as explained in Sections 3.1 and 3.2.

3.1. Discretisation

The cross-section to be investigated must first be divided into finite elements, to convert the continuous cross-section into the discrete approximation; the greater the number of discrete elements, the closer the numerical approximation is to the exact solution. Once the cross-section has been discretised into small elements and assigned co-ordinates (y_i,z_i) and an area A_i, the contribution for each can be summed to give the total cross-section response. Such a method is sometimes called a fibre analysis and has been used to analyse the cross-section behaviour of steel sections [16], concrete-filled steel tubes [9,24] and reinforced concrete sections.

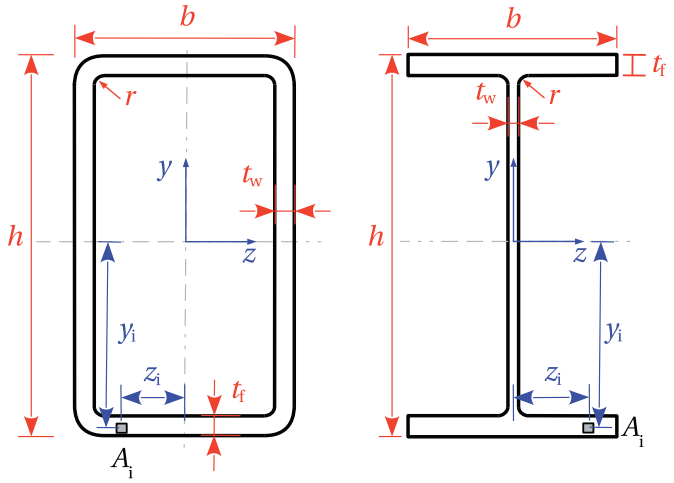

Fig. 3. Discretisation of rectangular hollow sections and I-sections.

For I-sections and rectangular hollow sections the definition of the elemental area A_i is straightforward, as the cross-section can be conveniently discretised into small rectangles. This can either be performed in strips that span the cross-section width or height, or by small elements that are organised across both the y and z directions of the cross-section, as shown in Fig. 3. Here, the root radii r are also explicitly included in the discretisation, as their effect can be significant.

Circular and elliptical hollow sections need to be treated in a different manner, since dividing either shape into small rectangular elements is not as ideal, as an error will arise at the curved edges of the cross-section. Circular hollow sections may be considered as a subset of elliptical hollow sections, and so the latter forms the basis of the necessary derivations. For the elliptical hollow section in Fig. 4, which has inner and outer dimensions a_1,a_2 and b_1,b_2 in the z and y directions respectively, an elemental area is not of constant shape as the inner and outer radii r_1 and r_2 are functions of angle θ. The area of an element A_i, contained by the rays at $\theta - \theta_i/2$ and $\theta + \theta_i/2$ either side of r (which is at an angle θ), and by the inner and outer radii r_a and r_b, is determined below.

The equation of an ellipse in polar co-ordinate form is that of Eq. (7), where a and b are the radii in the z and y directions respectively,

$$r = \frac{ab}{\sqrt{b^2\cos^2\theta + a^2\sin^2\theta}}. \tag{7}$$

The general area of a sector bounded by rays at angles θ_1 and θ_2 with curve r is

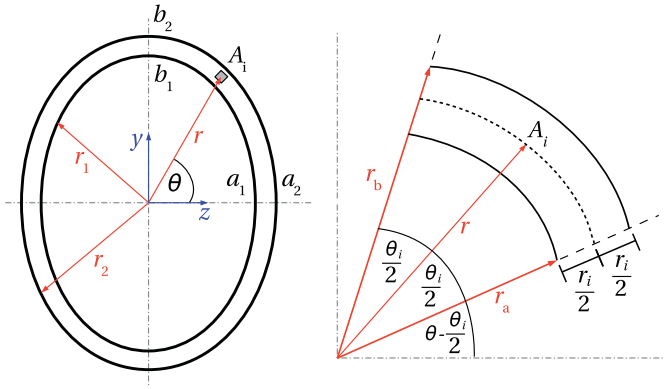

Fig. 4. Discretisation of an elliptical hollow section.

$$\frac{1}{2}\int_{\theta_1}^{\theta_2} r^2\,\mathrm{d}\theta = \frac{1}{2}\int_{\theta_1}^{\theta_2} \frac{a^2b^2}{b^2\cos^2\theta + a^2\sin^2\theta}\,\mathrm{d}\theta = \frac{ab}{2}\left[\arctan\left(\frac{a}{b}\tan\theta\right)\right]_{\theta_1}^{\theta_2}. \tag{8}$$

Introducing the function F simplifies the subsequent formulae

$$F = f(a, b, \theta) = \frac{ab}{2}\arctan\left(\frac{a}{b}\tan\theta\right). \tag{9}$$

By defining the elemental angle $\theta_i = 2\pi/m$ for m divisions around the ellipse, then $\theta_1 = \theta - \theta_i/2$ and $\theta_2 = \theta + \theta_i/2$. For the elemental length r_i in the radial direction, it is important to note that $r_i = r_b - r_a$ is not constant across θ_i as $r = f(\theta,a,b)$. With the thickness of the cross-section $t = a_2 - a_1 = b_2 - b_1$ split into n strips of length $\bar{r} = t/n$, the area A_i may be found by subtracting the area of the sector for $r_a = r - r_i/2$ from the area formed by $r_b = r + r_i/2$ to give

$$A_i = F\left(a+\tfrac{\bar{r}}{2},b+\tfrac{\bar{r}}{2},\theta+\tfrac{\theta_i}{2}\right) - F\left(a+\tfrac{\bar{r}}{2},b+\tfrac{\bar{r}}{2},\theta-\tfrac{\theta_i}{2}\right) - F\left(a-\tfrac{\bar{r}}{2},b-\tfrac{\bar{r}}{2},\theta+\tfrac{\theta_i}{2}\right) + F\left(a-\tfrac{\bar{r}}{2},b-\tfrac{\bar{r}}{2},\theta-\tfrac{\theta_i}{2}\right). \tag{10}$$

The general elliptical hollow section result for A_i may be preserved in this form. However for the case of a circular hollow section with $a = b = r$ it may be simplified further, as the function F can be simplified to give F_c as

$$F_c = \frac{r^2}{2}\arctan(\tan\theta) = \frac{r^2}{2}\theta, \tag{11}$$

which is the standard result of the sector area of a circle. For a circular hollow section, expanding and simplifying the general result for A_i gives $A_i = \bar{r}r\theta_i$.

3.2. Cross-section capacities

For the calculation of the axial load, major axis moment and minor axis bending moment acting on the cross-section, the following integration-to-discrete summed numerical approximations are used,

$$N = \int_A f\,\mathrm{d}A = \sum_i f_i A_i \tag{12}$$

$$M_y = \int_A fy\,\mathrm{d}A = \sum_i f_i y_i A_i \tag{13}$$

$$M_z = \int_A fz\,\mathrm{d}A = \sum_i f_i z_i A_i, \tag{14}$$

where y_i and z_i are the distances of the element centroid from the neutral axis of the cross-section in the y and z directions, f_i is the stress at the element, and A_i the elemental area. For major axis and minor axis bending, the strain at position y_i or z_i is

$$\epsilon_i = \frac{2y_i\epsilon_u}{h} \quad \text{and} \quad \epsilon_i = \frac{2z_i\epsilon_u}{b} \tag{15}$$

The stress f_i can then be determined from the material stress–strain curve that has been chosen.

For circular and elliptical hollow sections, it is convenient instead to use polar co-ordinates and evaluate the integral from the inner to outer radii and through an angle 2π when evaluating the bending moments. For a circular hollow section with $\mathrm{d}A = r\,\mathrm{d}\theta\,\mathrm{d}r$ and $y = r\sin\theta$, the moment integral can be converted to a numerical approximation using i as the index of the elements, and r_1, r_2 and r as the inner, outer and element radii respectively,

$$M = \int_{r_1}^{r_2}\int_0^{2\pi} fr^2\sin\theta\,\mathrm{d}\theta\,\mathrm{d}r = \sum_i f_i r^2\sin\theta\theta_i\bar{r}. \tag{16}$$

For an elliptical hollow section, r is no longer constant (as it is in the case of the circular hollow section case), and so the full A_i expression must be used. For the major axis moment

$$M = \sum_i f_i r\sin\theta A_i = \sum_i f_i \frac{ab\sin\theta}{\sqrt{b^2\cos^2\theta + a^2\sin^2\theta}}A_i. \tag{17}$$

For bending about the major and minor axes of an elliptical hollow section, the strain at element i is defined as

$$\epsilon_i = \frac{r\sin\theta\epsilon_u}{b_2} \quad \text{and} \quad \epsilon_i = \frac{r\cos\theta\epsilon_u}{a_2}, \tag{18}$$

and for a circular hollow section the elemental strain is

$$\epsilon_i = \frac{2r\sin\theta\epsilon_u}{D}. \tag{19}$$

For either the I-sections or tubular sections, it is important that a sufficient number of elements are used to represent the cross-section, such that the error in the approximations for the axial load and bending moment capacities is small. These approximation errors arise from a coarse representation of the geometry affecting y_i, z_i and A_i, particularly with regard to curved edges, leading to errors in ϵ_i or by using too few elements that assuming a constant strain and stress for an element is unreasonable. For this research, the flat plated elements are discretised in both the width and thickness directions, and for the circular and elliptical hollow sections through its thickness and around θ, until the values are accurate to within 0.1%. The accuracy can be determined by increasing the number of elements until a specified accuracy is achieved, or by comparing areas and second moment of areas to analytical solutions for the cross-section shapes.

4. *M–κ–N* curves

The first step needed to establish the moment–curvature–thrust curves is to create a suite of axial-bending interaction curves and record the curvature at points along each curve. The numerical model developed in Section 3 can be used to plot every discrete interaction of axial load and bending moment for any limiting strain, from pure bending to pure compression. The input data required to run each numerical step are the cross-section geometry, strain ratio (i.e. the ratio of the limiting strain to the yield strain) and stress–strain curve.

Two examples of *M–κ–N* curves, both employing the bi-linear material model for steel have been prepared: an I-section (a universal column with shape factors, defined as the ratio of the plastic to the elastic section moduli, of 1.18 and 1.51, about the major and minor axis, respectively) in bending about its minor axis is shown in Fig. 5 and a circular-hollow-section (with a shape factor of 1.41) is shown in Fig. 6. The strain ratio of 15 corresponds to the outer green line in both cases, and the moments and axial loads are normalised by the elastic values M_{el} (elastic moment) and N_y (yield load). For both suites of interaction curves, straight red lines indicate the axial–moment interactions when the cross-sections have not yielded, while the curves are more rounded with increasing deformation (increasing strain). The horizontal lines for a fixed axial load value of $N/N_y = 0.4$ are plotted, and gives a set of moment resistances at the intersections with each interaction curve. Not all interaction curves will be intersected by this line, since as the yield normalised axial load N/N_y increases, fewer associated partner moment possibilities occur.

The intersection moment values can be read from the interaction curves and plotted against the curvature; this curvature relates to the linearly varying strain components ϵ_B/ϵ_u in the numerical model. This procedure creates *M–κ* curves for a fixed axial load N/N_y, as plotted in Figs. 7 and 8 for the cross-sections of Figs. 5 and 6 and for a maximum curvature ratio κ/κ_y of 15, where κ_y is the curvature corresponding to the first yielding under bending alone. The curvature ratio κ/κ_y will always be less than the strain ratio when there is a coexistent, uniform strain ϵ_A, recalling that $\epsilon_A + \epsilon_B = \epsilon_u$ at failure. For both cross-section types, the gradient of the curves (which corresponds to the effective

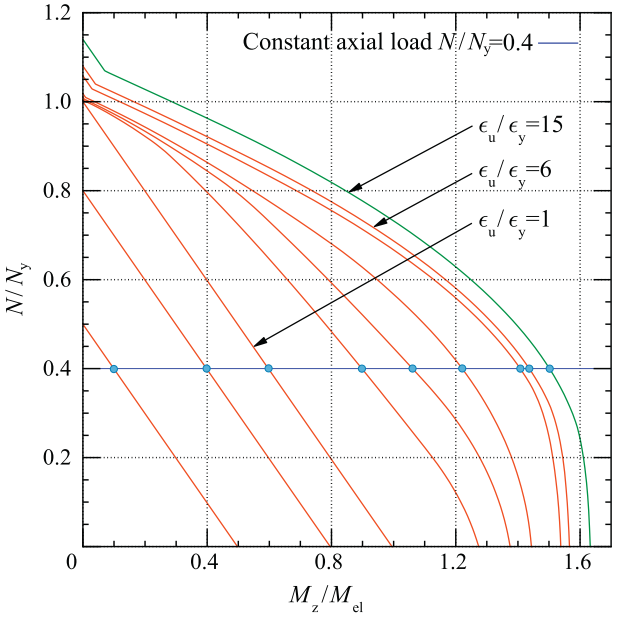

Fig. 5. Axial load and minor axis moment interaction curves for an I-section, with normalised outer fibre strain limits ϵ_u/ϵ_y = 0.5,0.8,1,2,3,4,5,6,15.

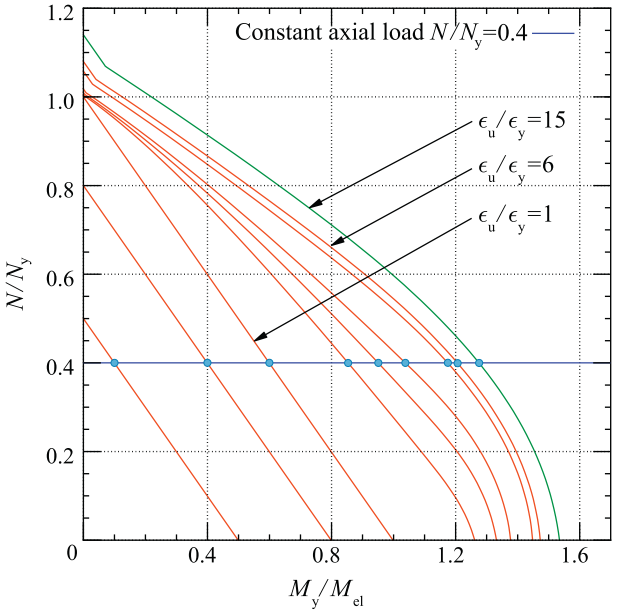

Fig. 6. Axial load and major axis moment interaction curves for a circular hollow section, with normalised outer fibre strain limits ϵ_u/ϵ_y = 0.5,0.8,1,2,3,4,5,6,15.

flexural rigidity $E'I$) starts from EI and reduces to $E_{sh}I$ (for the bi-linear material model) as curvatures increase. This transition occurs more slowly for cross-sections with higher shape factors due to the rate of stress redistribution throughout the cross-section. For $N/N_y \leq 0.2$, the effect on the moment–curvature curves of the I-section is very modest and remains small for $N/N_y \leq 0.4$ since the axial loads can be carried by the web, which is contributing relatively little to bending. Thereafter, increasing the axial load rapidly reduces the moment carrying capacity and the curves straighten. The circular hollow section shows similar behaviour, but is influenced more strongly by the rise in axial load.

5. Application

In this section the curves generated in Section 4 are applied to determine the equilibrium path, subject to presented assumptions, of a simply-supported (pin and roller) imperfect prismatic column subjected to an axial load. Note that the presence of an imperfection means that bending moments arise from the onset of loading - the member may therefore be considered to be a beam-column.

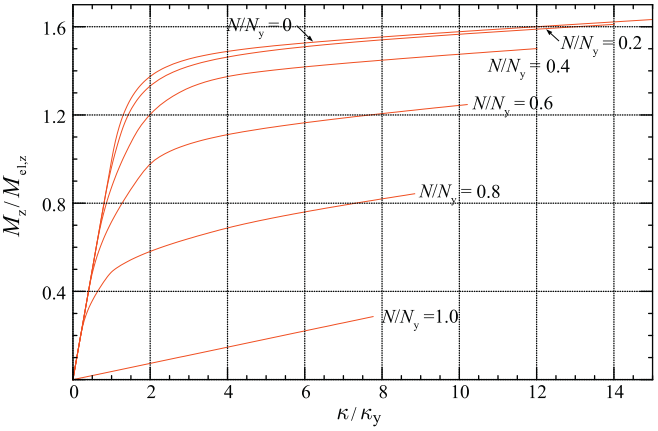

Fig. 7. Moment–curvature–thrust curves for an I-section, in minor axis bending.

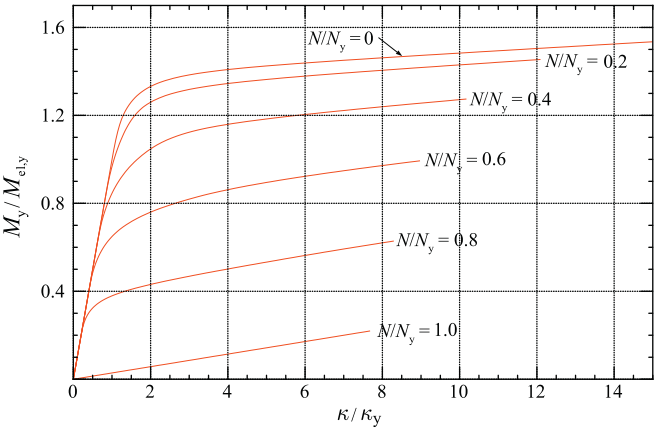

Fig. 8. Moment–curvature–thrust curves for a circular hollow section.

5.1. Structural system

A pin-ended prismatic column of length L is depicted in Fig. 9 which, in its unloaded state, has an imperfection $v_0(x)$ with maximum mid-height magnitude d_0. This function is an equivalent geometric imperfection distribution for the element, representing residual stresses and out-of-straightness. After the application of a concentric axial load N, a new total deflected shape $v_t = v + v_0$ (initial v_0 plus additional displacements v), which is in equilibrium with the applied axial load, has a maximum displacement at $x = L/2$ of $d_t = d + d_0$.

For a perfectly straight column where $d_0 = v_0 = 0$, the lowest elastic critical buckling load N_{cr} is given [25] by Eq. (20), where I_z is the minor axis second moment of area and L_z is the effective length. The corresponding deformed shape is a half sine wave with $v = d\sin(\pi x/L)$.

$$N_{cr} = \frac{\pi^2 EI_z}{L_z^2}. \tag{20}$$

This elastic critical buckling load value is shown in Fig. 10 as the horizontal line *Euler* for a column with global slenderness $\bar{\lambda} = \sqrt{N_y/N_{cr}} = 1$. This figure also depicts the other key curves in a normalised load–total lateral deflection format, as described below.

Assuming that the initial imperfect shape takes the form $v_0 = d_0 \sin(\pi x/L)$, the relationship between the axial load and the mid-height lateral deflection, can be written in the form of Eq. (21) [26]. This

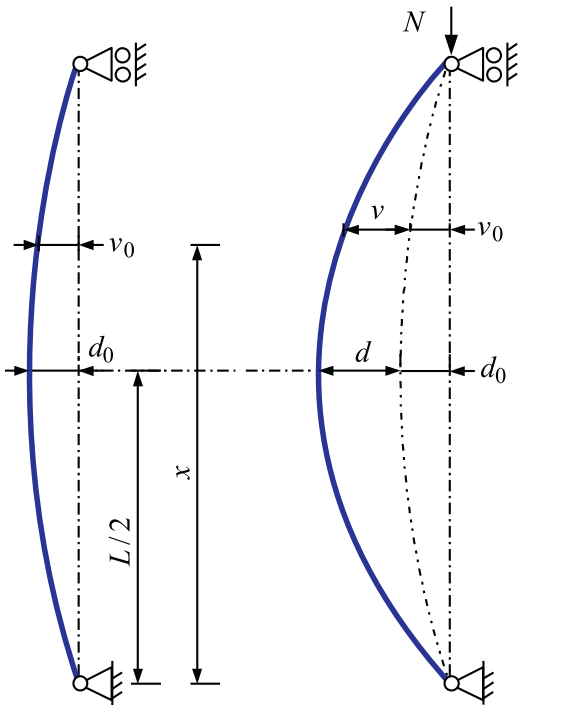

(a) Initial imperfection (b) Response under load

Fig. 9. Pin-ended and concentrically loaded imperfect column.

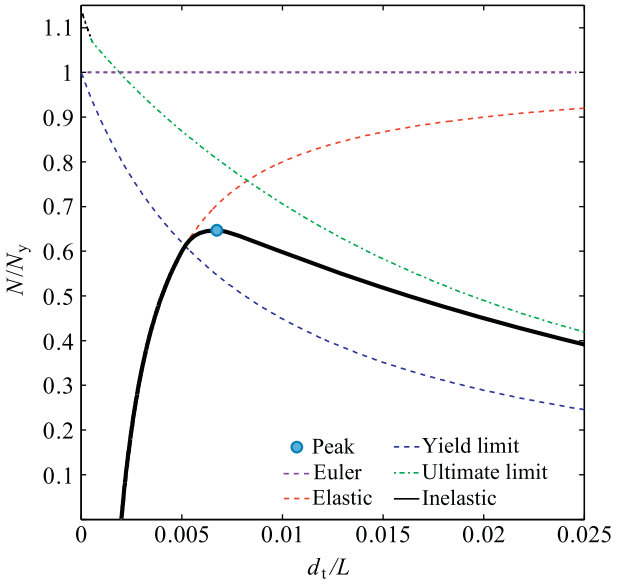

Fig. 10. Normalised load–lateral displacement curve for an imperfect column.

equation describes the elastic load–mid-height lateral deflection relationship, which is asymptotic to the Euler buckling load for $d_0 > 0$. This is plotted in Fig. 10 as curve *Elastic* for a given initial imperfection $d_0/L = 0.002$ at $x = L/2$.

$$\frac{N}{N_{cr}} = 1 - \frac{d_{0,z}}{d_{t,z}} \tag{21}$$

This *Elastic* curve in Fig. 10 highlights a fundamental characteristic of the imperfect column system, which is the amplification of lateral deflections due to geometric effects. This is because on the application of the concentric axial load N, a bending moment distribution $M(x) = Nv_t(x)$ is formed throughout the column height. This creates further lateral deflections, which in turn creates additional bending moments, and the process continues until equilibrium is achieved. These geometric second order effects mean that the flexural rigidity which provides the stiffness to oppose the lateral deflections, becomes an important variable, as the deformed geometry provides feedback into the system.

Further complicating the response of the column is that the elastically derived equations are only valid while the material stresses and strains are below the yield values ($f \le f_y$ and $\epsilon \le \epsilon_y$), while in practice the inelastic behaviour of the material, such as its strain hardening potential and failure strains are also important. A yield limited approach which offers an estimate of the axial load-carrying capacity, assuming that the cross-section will not buckle locally before first yield, is found by tracing the elastic path of Eq. (21) until $f = f_y$ is reached at the most stressed outer-fibres. This occurs when axial compressive stresses combine with the bending compressive stresses on the concave side of the column, and is commonly represented by the Perry–Robertson formula given by Eq. (22),

$$\frac{N}{N_y} = \frac{1}{2}\left[1+\frac{N_{cr}}{N_y}(1+\eta_e)\right] - \frac{1}{2}\sqrt{\left[1+\frac{N_{cr}}{N_y}(1+\eta_e)\right]^2 - 4\frac{N_{cr}}{N_y}} \tag{22}$$

with $\eta_e = Ad_0/W_{el}$. This is plotted in Fig. 10 as the *Yield limit* curve, for a suite of d_0 (initial imperfection) values.

An upper bound N–d_t curve can be found based on the cross-section limiting strain ϵ_u by using $d_t = M/N$ and dividing each moment on the N–M interaction curves by the axial loads N. This represents the ultimate cross-section capacity with no influence from global effects. This upper bound curve is plotted in Fig. 10 for a strain ratio of 15 as *Ultimate limit*.

The actual response (within the assumptions of the problem setup), is plotted in Fig. 10 as the curve *Inelastic*, and begins at $N = 0$ and $d_t = d_0$, and initially follows the *Elastic* curve until the *Yield limit* curve is reached, indicating first yielding at $x = L/2$. After the first yield point, the flexural rigidity will quickly deteriorate at $x = L/2$ as the material plastically deforms, but some additional load up until the peak load N_u can still be carried. After this inelastic peak load, which is plotted in Fig. 10 as *Peak*, the column can no longer be in equilibrium for an increase in axial load N, and so an unloading path is followed and associated with further lateral deflections. This unloading continues until the *Ultimate limit* curve is reached, when the strains at the critical mid-height cross-section reach the limiting strain ϵ_u and the cross-section fails locally. The difficulty in finding the peak load N_u, is that beyond the first yield point a combination of geometric effects and material non-linearity combine to deteriorate the flexural stiffness of the column. It is here that the cross-section flexural stiffness can be introduced from the curves generated in Section 4 to help solve the problem.

5.2. Numerical solution

A variety of numerical solutions exist in finding the load-deflection behaviour of members subject to compression and first or second order bending [2,27]; here, the fundamental static-equilibrium equation will be paired with the M-κ-N curves to form a solution. It is important to outlay some of the assumptions utilised in this approach: 1) pinned boundary conditions at the column ends; 2) shear deformations are not influential in the lateral deformations, and so the method is not applicable to short members; 3) load reversal is not considered and the solution for a given applied load does not depend on the stress states at the previous applied loading level; 4) deformations are not excessive such that the inclination of the internal axial load meets the supports far from vertical (which for the example problem is satisfied at peak load and soon after), 5) residual stresses are not explicitly included but may be represented by an enhanced initial imperfection amplitude, and 6) axial strains are not significant such that the member can be considered

inextensible at length L.

The differential equation given by Eq. (23) describes the equilibrium between an external applied moment M, and the internal resisting moment $\bar{E}I\kappa$, where $\bar{E}I$ represents the elastic or inelastic flexural stiffness, through an effective Young's modulus $\bar{E}$, and curvature κ adopts its large deflection definition.

$$\bar{E}I\kappa = \bar{E}I\frac{\frac{d^2v}{dx^2}}{\left[1+\left(\frac{dv}{dx}\right)^2\right]^{\frac{3}{2}}} = -M. \tag{23}$$

For a pin-ended compression member of length L there exists boundary conditions $v(0) = 0$ and $v(L) = 0$. Eq. (23) is a boundary valued, nonlinear, second order, ordinary differential equation that can be formatted into two first order, ordinary differential equations with $M = Nv_t = N(v_0 + v)$ and for a given axial load and initial mid-height deflection d_0. This gives Eqs. (24) to (26):

$$v_1 = v \tag{24}$$

$$v_2 = \frac{dv_1}{dx} = \frac{dv}{dx} \tag{25}$$

$$\frac{dv_2}{dx} = \frac{d^2v}{dx^2} = -\frac{N(v_0+v_1)}{\bar{E}I}(1+v_2^2)^{\frac{3}{2}}. \tag{26}$$

The key complication in this formulation is that $\bar{E}I$ is itself a function of curvature, which includes the highest derivative d^2v/dx^2 and also varies with x. Recall that the gradient of a cross-section's moment–curvature curve gives the effective flexural rigidity; this is the first derivative of the moment–curvature function with respect to curvature. The effective flexural rigidity provides information on the ability of the cross-section to carry additional bending based on its current elastic or inelastic state. For every (M,κ,N) point on the moment–curvature–thrust curves, the gradient $\bar{E}I$ is calculated. $\bar{E}I$ can be posed as a function of the total deflection so that $\bar{E}I = f(v_t)$ as deflections will be solved for in the ODE. Therefore we can plot $\bar{E}I$ against $v_t = M/N$, as M and N are known for all positions on a given curve. This is a powerful feature of using moment–curvature–thrust curves, in that they can be transformed readily into the format needed for the particular analysis. This gives the effective flexural rigidity–total deflection curves of Fig. 11.

The effective flexural rigidity starts at the elastic value $\bar{E}I = EI$ and stays constant while the cross-section is elastic, before dropping sharply as the cross-section yields and more material switches from a stiffness of $\bar{E} = E$ to $\bar{E} = E_{sh}$. This transition between two stiffness values is a consequence of using a bi-linear material model; material models with different characteristics will give different curves, so for example, a rounded stress–strain curve will give a smoother degradation of stiffness $\bar{E}I$. The generated $\bar{E}I$–v_t plots allow $\bar{E}I$ in Eq. (26) to be replaced with the function $f(v_t) = f(d_0 \sin(\pi x/L) + v_1)$, which gives Eq. (27). The function $f(v_t)$ is formed by linearly interpolating between the discrete data points from Fig. 11, with many datapoints used along the curve for improved interpolation accuracy.

$$\frac{dv_2}{dx} = -\frac{N[d_0 \sin(\pi x/L)+v_1]}{f(d_0 \sin(\pi x/L)+v_1)}(1+v_2^2)^{\frac{3}{2}}. \tag{27}$$

The differential equation is now in a format to be solved, with the solution presented here derived using MATLAB [28] with the boundary valued ordinary differential equation solver function BVP4C.m. The resulting accuracy of the solutions is set to a relative error of 0.1%. The results are for a universal column cross-section buckling about the minor axis, with $d_0/L = 1/250$ and $\bar{\lambda} = \sqrt{N_y/N_{cr}} = 1$ and giving a peak load (marked with a dashed red line in the following figures) of $N_u = 0.557N_y$. The direct results from the solution of the ODE are v_1 and v_2, which are the lateral displacements v and the slopes θ at each point along the member height.

The normalised lateral displacements v along the member length are plotted in Fig. 12. It can be seen that, as a consequence of the linear elastic material response up to f_y, the member assumes a sinusoidal deflected shape until first yield and also a close approximation to a sine shape at the peak load (highlighted with the dashed line). The deformed shape then becomes more pointed during the post-peak unloading phase as the mid-height cross-section loses its flexural rigidity due to material yielding and lateral deflections increasing rapidly.

For the slope θ in Fig. 13, a cosine function as the derivative of the sine displacements is observed for the elastic region until a sharp change of slope is witnessed at mid-height as the cross-section yields. As the second derivative, the curvature appears again as a sine function for the elastic case in Fig. 14. Since curvature κ is not a direct result of the ODE analysis, it is found by calculating the slope of the θ—x/L plot. The presence of a yielding zone between approximately $x/L = 0.4$ and $x/L = 0.6$ is apparent in this plot as a spike of curvature values.

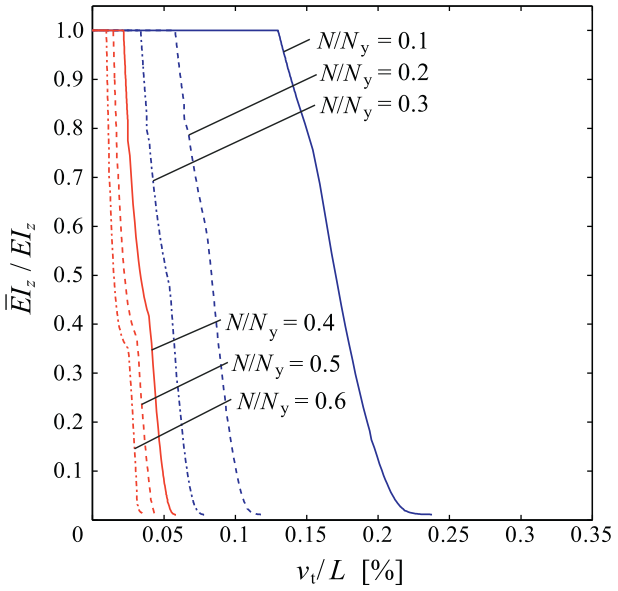

Fig. 11. Curves for $\bar{E}I$–v_t–N derived from M–κ–N curves, for minor axis bending of an I-section with a bi-linear material model.

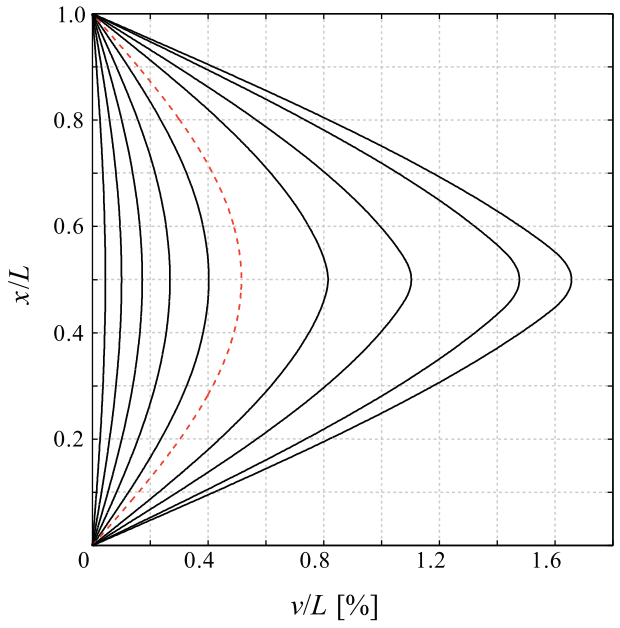

Fig. 12. Displacements from the BVP4C solution of an I-section UC under increasing axial load (dashed line indicates $N = N_u$). (For interpretation of the references to colour in this figure, the reader is referred to the web version of this article.)

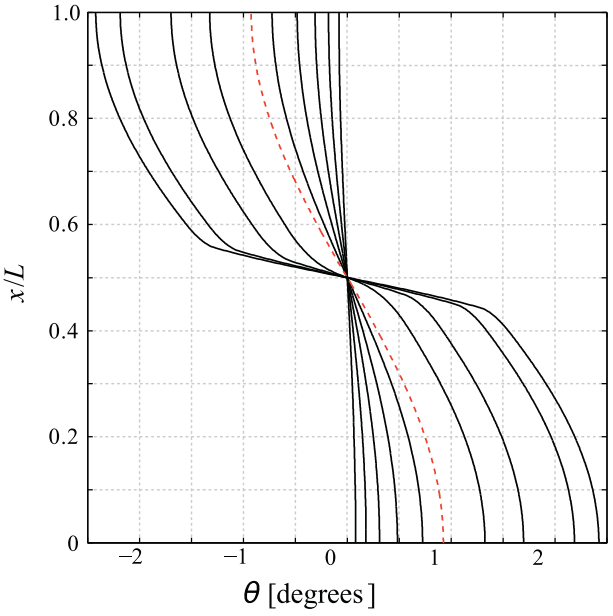

Fig. 13. Rotations from the BVP4C solution of an I-section UC under increasing axial load (dashed line indicates $N = N_u$). (For interpretation of the references to colour in this figure, the reader is referred to the web version of this article.)

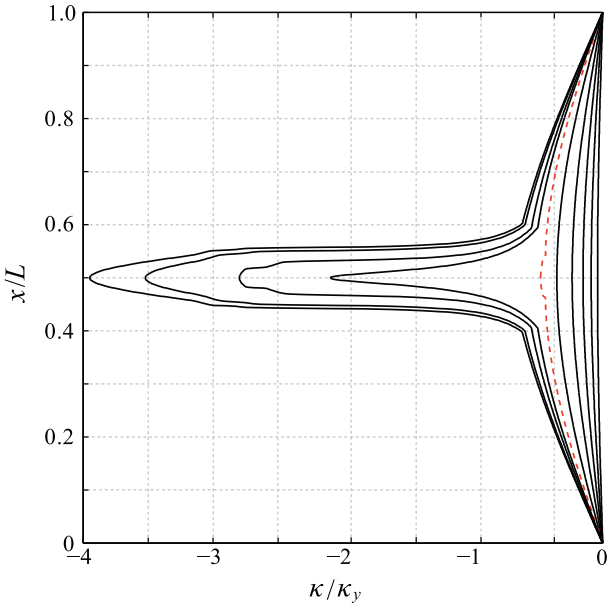

Fig. 14. Curvatures from the BVP4C solution of an I-section UC under increasing axial load (dashed line indicates $N = N_u$). (For interpretation of the references to colour in this figure, the reader is referred to the web version of this article.)

Fig. 15 shows the distribution of yielding at the peak load ($N = 0.557N_y$) and during the unloading phase for $N = 0.50N_y$, $N = 0.45N_y$, $N = 0.40N_y$. The plots illustrate the stress magnitude distribution throughout the member, with the areas of lower stress in black and the areas that have yielded displayed in white. The concave side of the member is on the right-hand-side; this is where the compressive stresses from the axial load and the bending moment combine to cause first yielding on the inner-face.

The stress distribution at peak load shows that the majority of the member is still elastic, with yielding confined to the inner surface at mid-height. Yielding expands to cover a wide hinge region between $x/L = 0.4$ and $x/L = 0.6$, with the distribution of yielding becoming closer to symmetric about the cross-section as flexure in the unloading stages becomes increasingly dominant due to the greater ($M = Nv_t$) second order effects.

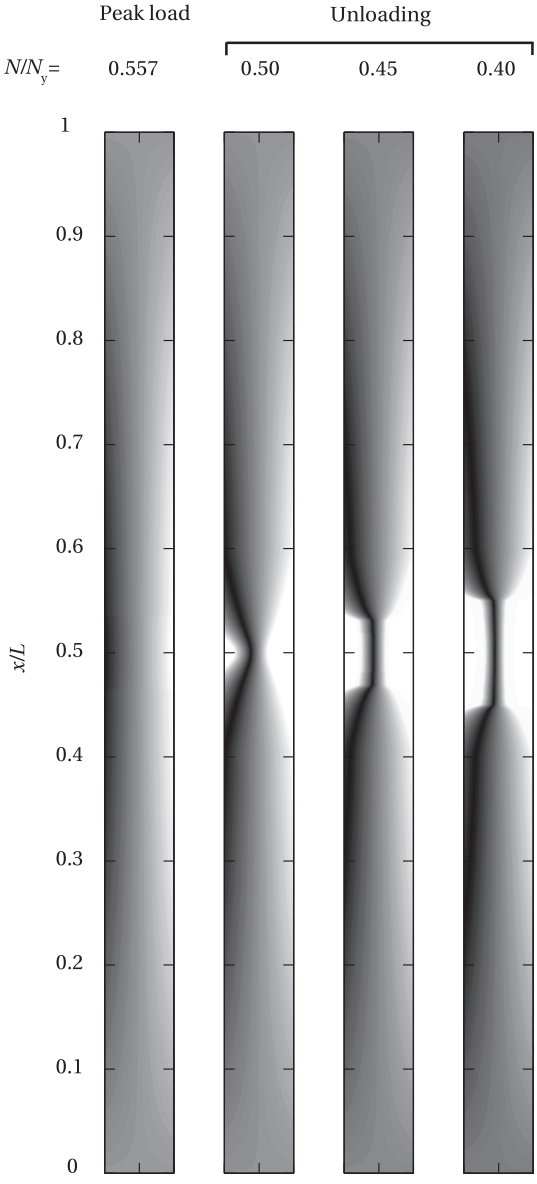

Fig. 15. Stress distribution at the peak load and during unloading for a member showing a distinct yield zone or plastic hinge (compression side to the right).

6. Conclusions

Moment-curvature-thrust curves provide useful data to assist in the solution of a variety of inelastic and geometrically non-linear structural problems involving beam-columns. Information on deflections, curvatures and stress or strain distributions can be found by discretising the beam-column and, using the M–κ–N curves, integrating over the member length. The M–κ–N curves are generated numerically in this paper.

The method involves defining a linear strain distribution throughout the cross-section, based on the superposition of a uniform strain and a linearly varying strain representing pure compression and flexure, respectively. The strain distribution is limited by a local buckling strain based on the Continuous Strength Method, which designates a compressive ultimate strain to signal the attainment of the ultimate strength of the cross-section by elastic or inelastic local buckling. The local buckling strain can be predicted from CSM base curves derived from experimental observations. The cross-section to be analysed must be

first discretised and the strength then calculated by appropriate integration/summations over the elements from the stress and strain profiles, where the stresses are determined from the driving strain distribution and the chosen material model.

The pairing of axial load and bending moment values leads to cross-section interaction curves, for the given limiting failure strain. These are shown herein for steel I-sections bending about either the major or minor axis and circular hollow sections, but the general strain driven approach can to applied to a far wider variety of cross-section shapes and materials. By drawing a constant axial load line intersecting these curves, all of the moment and curvature data can be extracted, giving the information to produce the M–κ–N curves. These curves show how the moment that the cross-section can endure, varies with the axial load level, and the curvature (deformation) that is needed. The gradient of the curves gives the inelastic effective flexural stiffness $\bar{E}I$, which is an important parameter in numerical methods and used to calculate deflections. A unique characteristic of the method, is that by defining the limiting cross-section strain with the Continuous Strength Method, local buckling can be captured and hence the moment-curvature-curves implicitly include a termination point related to the strength of the cross-section. Application of the moment–curvature–thrust curves to the solution of a beam-column problem is demonstrated by means of an example, in which the full load–deformation history of the member could be successfully traced.

References

[1] Byfield, Nethercot. An analysis of the true bending strength of steel beams. Proc. Inst. Civ. Eng. Struct. Build. 1998;128:188–97.
[2] Chen, Atsuta. Theory of beam-columns - volume 1: in-plane behavior and design. McGraw-Hill; 1976.
[3] Chen, Ashour, Garrity. Moment-thrust interaction diagrams for reinforced masonry sections. Constr Build Mater 2008;22(5):763–70.
[4] Chen, Sugimoto. Moment-curvature-axial-compression-pressure relationship of structural tubes. J Constr Steel Res 1985;5:247–64.
[5] Duan, Chen, Loh. Analysis of dented tubular members using moment curvature approach. Thin-Walled Struct 1993;15:15–41.
[6] Kim, Ostapenko. A simplified method to determine the moment-curvature relationships of a damaged tubular segment. Eng Struct 1996;18(5):387–95.
[7] Kwak, Kim. Nonlinear analysis of RC beams based on moment-curvature relation. Comput Struct 2002;80:615–28.
[8] Haedir, Zhao, Grzebieta, Bambach. Non-linear analysis to predict the moment-curvature response of CFRP-strengthened steel CHS tubular beams. Thin-Walled Struct 2011;49:997–1006.
[9] Montuori, Piluso. Analysis and modelling of CFT members: moment curvature analysis. Thin-Walled Struct 2015;86:157–66.
[10] Portolés, Romero, Filippou, Bonet. Simulation and design recommendations of eccentrically loaded slender concrete-filled tubular columns. Eng. Struct. 2011;33(5):1576–93.
[11] Frangopol, Ide, Spacone, Iwaki. A new look at reliability of reinforced concrete columns. Struct. Saf. 1996;18:123–50.
[12] Spacone, Filippou, Taucer. Fibre beam-column model for non-linear analysis of RC frames: part I formulation. Earthq. Eng. Struct. Dyn. 1996;25:711–25.
[13] Gardner. The continuous strength method. Proc. Inst. Civ. Eng. Struct. Build. 2008;161:127–33.
[14] Liew. Design of structural steel elements with the continuous strength method. Imperial College London: Department of Civil and Environmental Engineering; 2014. PhD thesis.
[15] 1993-1-1. Eurocode 3: design of steel structures - part 1-1: general rules and rules for buildings. European Standard 2005:1–96. CEN.
[16] Liew, Gardner. Ultimate capacity of structural steel cross-sections under compression, bending and combined loading. Structures 2015;1:2–11.
[17] 1993-1-5. Eurocode 3: design of steel structures - part 1-5: plated structural elements. European Standard 2006:1–53. CEN.
[18] Gardner, Wang, Liew. Influence of strain hardening on the behavior and design of steel structures. Int. J. Struct. Stab. Dyn. 2011;11(5):855–75.
[19] Zhao, Afshan, Gardner. Structural response and continuous strength method design of slender stainless steel cross-sections. Eng. Struct. 2017;140:14–25.
[20] Afshan, Gardner. The continuous strength method for structural stainless steel design. Thin-Walled Struct. 2013;68:42–9.
[21] Su, Young, Gardner. Testing and design of aluminum alloy cross-sections in compression. J. Struct. Eng. ASCE 2014;140(9). UNSP 04014047.
[22] Su, Young, Gardner. The continuous strength method for the design of aluminium alloy structural elements. Eng Struct 2016;122:338–48.
[23] Buchanan, Gardner, Liew. The continuous strength method for the design of circular hollow sections. J Constr Steel Res 2016;118:207–16.
[24] Choi, Kim, Choi. Simplified P-M interaction curve for square steel tube filled with high-strength concrete. Thin-Walled Struct 2008;46:506–15.
[25] Euler. Methodus Inveniendi Lineas Curvas Maximi Minimive Proprietate Gaudentes. Lausanne and Geneva: Appendix: De curvis elasticis; 1744.
[26] Timoshenko, Gere. Theory of elastic stability. 2nd ed. McGraw-Hill; 1961.
[27] Bleich. Buckling strength of metal structures. McGraw-Hill; 1952.
[28] MATLAB Version, 8.5 (R2015a). The MathWorks Inc. Massachusetts: Natick; 2015.